Article

Realizing Two-Dimensional Supramolecular Arrays of a Spin Molecule via Halogen Bonding

Dingguan Wang,* Zishen Wang, Shaofei Wu, Arramel, Xinmao Yin, Chi Sin Tang, Yuan Ping Feng, Jishan Wu,* and Andrew T. S. Wee*

Read Online

ACCESS | 📊 Metrics & More | 📖 Article Recommendations | 🆘 Supporting Information

ABSTRACT: Well-ordered spin arrays are desirable for next-generation molecule-based magnetic devices, yet their synthetic method remains a challenging task. Herein, we demonstrate the realization of two-dimensional supramolecular spin arrays on surfaces via halogen-bonding molecular self-assembly. A bromine-terminated perchlorotriphenylmethyl radical with net carbon spin was synthesized and deposited on Au(111) to achieve two-dimensional supramolecular spin arrays. By taking advantage of the diversity of halogen bonds, five supramolecular spin arrays form and are probed by low-temperature scanning tunneling microscopy at the single-molecule level. First-principles calculations verify that the formation of three distinct types of halogen bonds can be used to tailor supramolecular spin arrays via molecular coverage and annealing temperature. Our work suggests that supramolecular self-assembly can be a promising method to engineer two-dimensional molecular spin arrays.

KEYWORDS: organic radicals, 2D spin arrays, molecular self-assembly, halogen bonds, scanning tunneling microscopy, DFT calculations
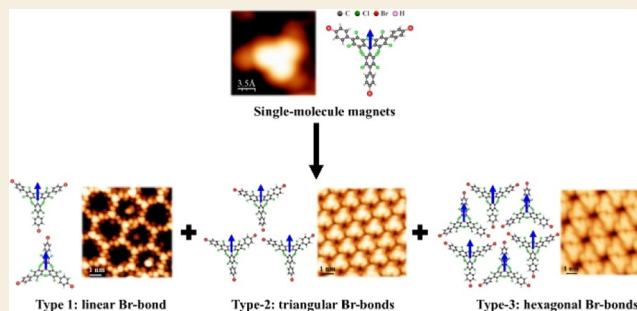
Single-molecule magnets (SMMs) are magnetic entities composed of a single molecule with net spin. SMMs have attracted much interest due to their potential applications in ultrahigh-density information storage,[1,2] quantum computers,[3,4] and spintronic devices.[5,6] Metal−organic compounds consisting of transition metals and organic ligands are the research focus of SMMs, and various types of metal−organic magnets have been reported.[7−11] Unlike metal spins, which originate from the unpaired electrons in the *d*- or *f*-orbital, organic carbon is another spin element that generates its magnetism due to an unpaired electron in the *p*-orbital. Recent studies have shown that through molecular design, organic molecules could exhibit an open-shell ground state, revealing emergent SMMs with a net carbon spin.[12−16]

The successful synthesis of high-quality SMMs enables further research on molecule-based magnetic devices. Fabricating ordered spin arrays of SMMs is an important step toward practical applications. Crystal engineering can be used to impart control over the ordered molecular architectures and align the spin orientation/distance of SMMs into one-, two-, or three-dimensional spin arrays such that spin-exchange interaction and the resulting magnetic properties can be tuned efficiently.[14,17−19] In particular, the realization of two-dimensional (2D) spin arrays on a substrate has attracted much interest due to their potential applications in next-generation magnetic devices.[20] Until now, several reports have demonstrated 2D molecular spins via the deposition of

SMMs[21,22] or on-surface synthesis of molecular magnets on a substrate.[23−28] However, due to the lack of an effective means to regulate the molecular arrangement, it is still a challenge to achieve highly ordered 2D molecular spin arrays on the surface.[29,30] Molecular self-assembly on surfaces has shown many advantages in achieving 2D supramolecular arrays.[31−35] Utilizing various intermolecular interactions, many 2D ordered supramolecular arrays have been reported.[36−42] In particular, by employing high-resolution surface characterization techniques, halogen bonds have recently been studied and show great promise in mediating ordered supramolecular arrays on surfaces.[43−46]

In this work, a bromine-terminated perchloro-triphenylmethyl radical (3Br-PTM) with net carbon spin is synthesized and thermally deposited to achieve 2D ordered molecular spin arrays on an insulating bromine monolayer on Au(111). Halogen bonds play an important role in regulating the supramolecular spin arrays formed on the surface. By taking advantage of the diversity of halogen bonds, five ordered supramolecular arrays with variable molecular spin densities
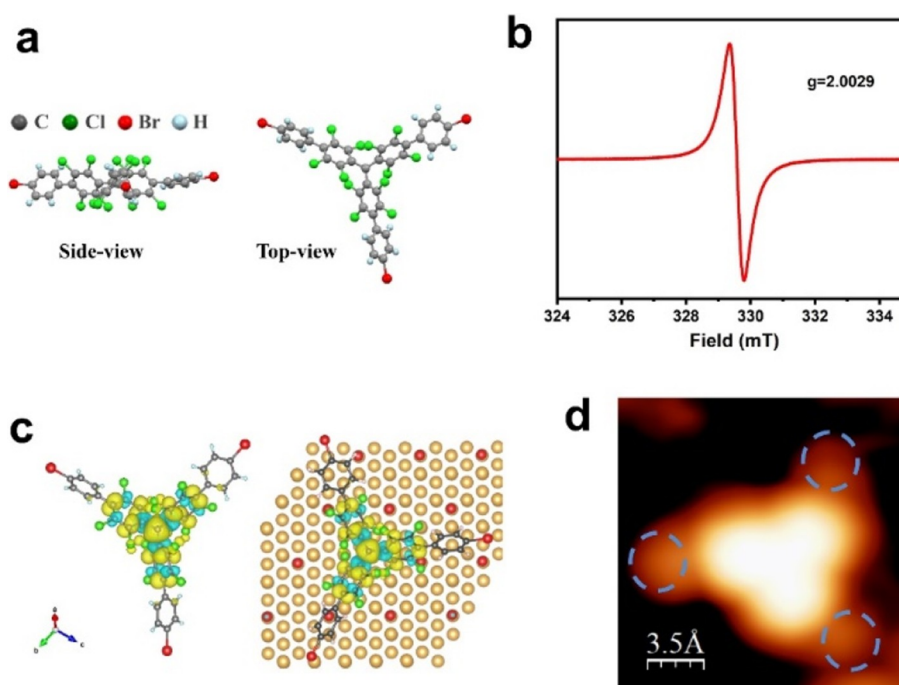
Figure 1. Molecular spin originating from an unpaired electron in the central carbon of the 3Br-PTM molecule. (a) Chemical structure of the 3Br-PTM molecule and the side view and top view of the 3Br-PTM molecule are obtained from single-crystal XRD. (b) ESR spectrum of the 3Br-PTM sample at 293 K, and a g value of 2.0029 indicates a typical carbon-centered spin. (c) Calculated spin density distribution of the 3Br-PTM molecule in the gas phase (left) and on the surface (right); yellow and light-blue isosurfaces indicate spin-up and spin-down, respectively. (d) High-resolution STM image of a single 3Br-PTM molecule on Au(111), three outer Br-terminated benzene rings are labeled by light-blue circles, set point: V_{tip} = −0.2 V and I_{tip} = 38 pA.
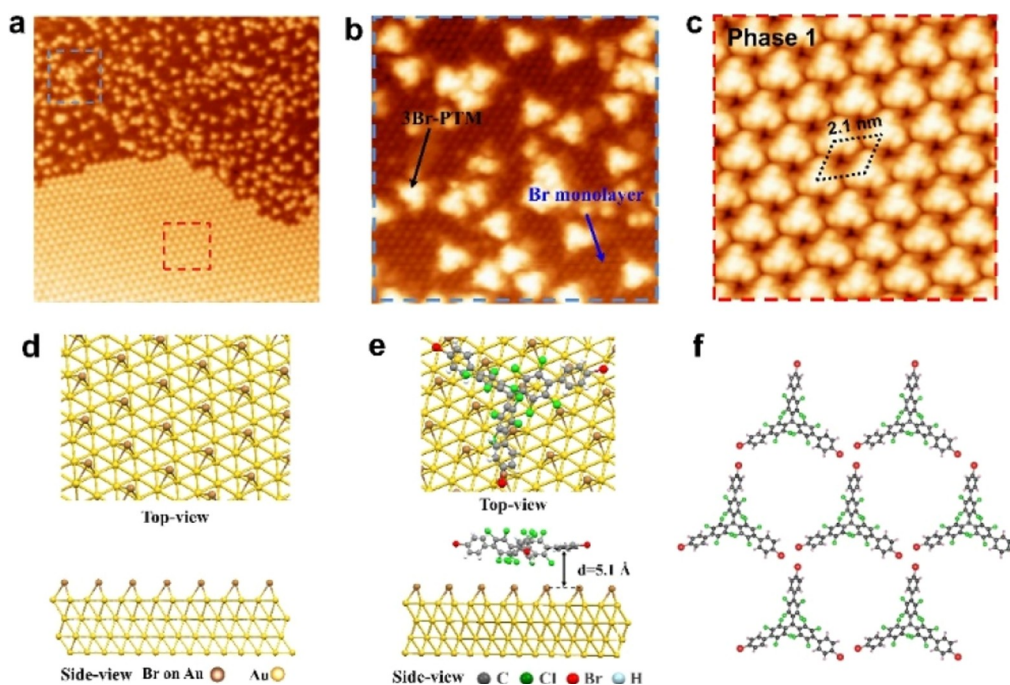

Figure 2. 3Br-PTM sub-monolayer/Br-monolayer/Au(111). (a) STM image of the 3Br-PTM sub-monolayer on the Br monolayer/Au(111) after depositing it at 180 °C for 3 min, set point: V_{tip} = 1.0 V and I_{tip} = 30 pA, size: 60 nm × 60 nm. (b) Enlarged STM image of a few 3Br-PTM molecules on the Br-monolayer on Au(111), set point: V_{tip} = 1.0 V and I_{tip} = 30 pA, size: 15 nm × 15 nm. (c) Enlarged STM image of phase-1 domain; set point: V_{tip} = 0.8 V and I_{tip} = 30 pA; size: 10 nm × 10 nm, lattice parameter = 2.1 nm. (d) Calculated Br-monolayer on Au(111), unit cell: 0.54 nm × 0.54 nm; Br atoms absorb on the hexagonal close-packed (hcp) site, and by contrast, the Br monolayer is energetically unstable when absorbed on the face-centered cubic site. (e) Calculated atomic structure of a 3Br-PTM molecule on the Br-monolayer on Au(111). (f) DFT-optimized molecular packing structure of the phase-1 domain.
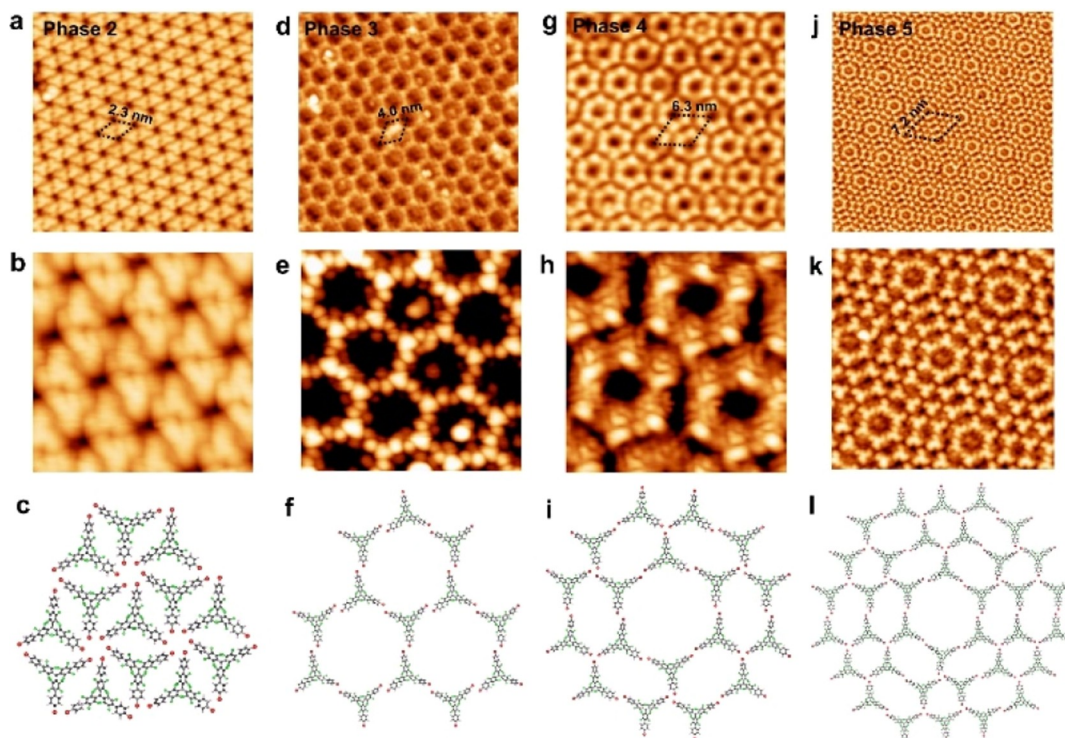
Figure 3. Multiphases of 3Br-PTM self-assembled on the Br-monolayer on Au(111). (a–c) STM images and DFT-optimized structure of phase-2 at high coverage at room temperature; set point: (a) V_{tip} = −0.2 V, I_{tip} = 25 pA, size: 25 nm × 25 nm, and lattice parameter = 2.3 nm; (b) V_{tip} = −0.5 V, I_{tip} = 25 pA, and size: 8 nm × 8 nm. (d–f) STM images and DFT-optimized structure of phase-3 at high coverage; set point: (d) V_{tip} = 0.8 V, I_{tip} = 30 pA, size: 25 nm × 25 nm, and lattice parameter = 4.0 nm; (e) V_{tip} = 0.5 V, I_{tip} = 21 pA, and size: 8 nm × 8 nm. (g, h, i) STM images and DFT-optimized structure of phase-4 at high coverage; set point: (g) V_{tip} = 1.2 V, I_{tip} = 54 pA, size: 25 nm × 25 nm, and lattice parameter = 6.3 nm; (h) V_{tip} = −1.5 V, I_{tip} = 130 pA, and size: 8 nm × 8 nm. (j–l) STM images and proposed molecular packing structure of phase-5 observed after annealing at 250 °C; set point: (j) V_{tip} = 0.8 V, I_{tip} = 29 pA, size: 50 nm × 50 nm, and lattice parameter = 7.2 nm; (k) V_{tip} = 0.8 V, I_{tip} = 29 pA, and size: 18 nm × 18 nm. Since the substrate does not play a crucial role in determining the self-assembled phases and in order to simplify the computational work, we did not include the substrate in our calculated models of the five phases.

and distances are observed using high-resolution low-temperature scanning tunneling microscopy (LT-STM). Density functional theory (DFT) calculations further show that the observed molecular spin arrays are mainly governed by three distinct types of halogen bonds, namely, single Br-bond (type-1 halogen bond), triangular Br-bonds (type-2 halogen bond), and hexagonal Br-bonds (type-3 halogen bond).

The 3Br-PTM molecule was synthesized via solution-based organic synthesis (Figure S1 in the Supporting Information). Figure 1a displays a three-dimensional molecular structure of 3Br-PTM that was obtained from single-crystal X-ray diffraction (XRD) (CCDC 2088008). The 3Br-PTM backbone is a triangular-shaped molecule with D$_3$ symmetry. The 3Br-PTM is a nonplanar molecule since its two adjacent benzene rings are rotated with respect to the plane of the molecule due to steric hindrance.

Since the 3Br-PTM molecule has an odd number of sp^2 carbons (37 carbons), an electron in the p-orbital of the central carbon does not participate in the pairing π-bonds, which leads to the formation of carbon-centered net spin.[47] To verify our hypothesis, electron spin resonance (ESR) measurements were carried out. As shown in Figure 1b, an intense ESR signal is observed with a g value of 2.0029, suggesting a typical carbon-centered spin. DFT calculations also support the ESR observation. Figure 1c (left) shows the calculated spin density distribution of a 3Br-PTM molecule in the gas phase, which shows that the spin is mainly localized at the central carbon atom. Moreover, a spin intensity of 1.0 μB per molecule is

obtained. Previous reports have shown that the carbon spin can be retained on the metal surface.[48,49] Our DFT calculations also suggest magnetic retention on the surface. Figure 1c (right) shows the calculated spin density distribution of the 3Br-PTM molecule on the surface, which suggests a reserved carbon-centered spin. According to the calculated results, the magnetic strength of 3Br-PTM on Au(111) is 0.24 μB per molecule. We note that this magnetic strength on the surface is lower than that in the gas phase, suggesting a shielding effect from the substrate. We propose that the shielding effect is due to charge transfer, as suggested by DFT calculation in Figure 1c (right).

Figure 1d exhibits a high-resolution STM image of a single 3Br-PTM molecule on Au(111). The molecule presents a triangular geometry with D$_3$ symmetry, consistent with our observation in the single-crystal XRD determination in Figure 1a. Due to the out-of-plane feature of the adjacent benzene rings (the outer and inner benzene rings), their STM contrast variation reflects that the three outer bright spots are assigned to the outer Br-terminated benzene rings (labeled by blue circles), while the other three are brighter spots (clover-like structure) associated with the three inner benzene rings.

Figure 2 presents the vertically stacked heterostructures consisting of the 3Br-PTM sub-monolayer on the Br-atom monolayer on the Au(111) substrate. Figure 2a shows a low-molecular-coverage STM image obtained via depositing the 3Br-PTM molecule on Au(111). Two distinct domains are observed: one domain is covered by Br atoms, while another is
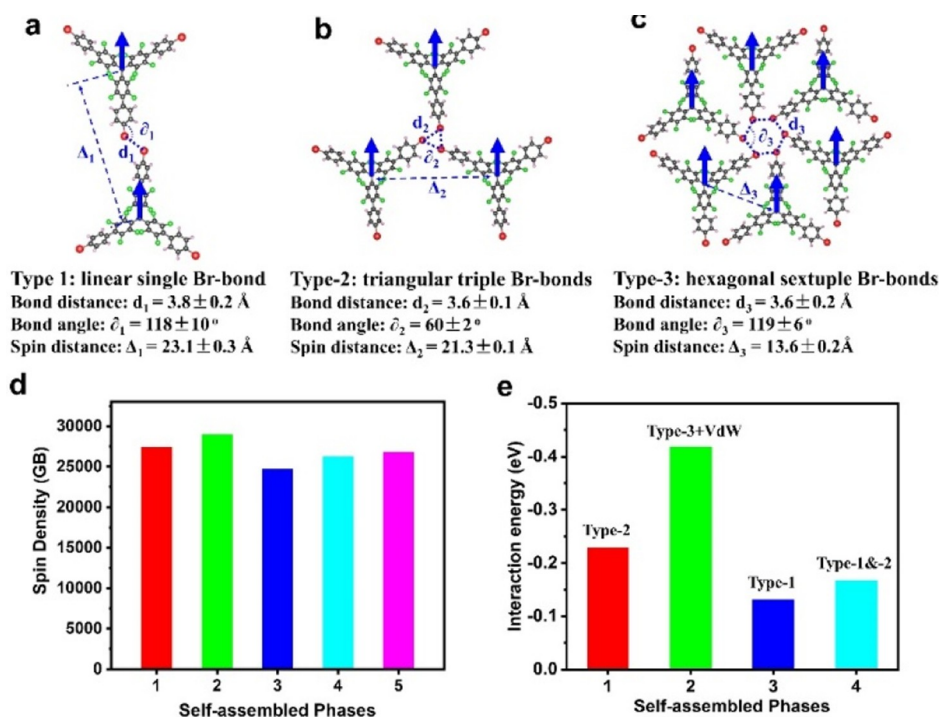
Figure 4. Formation of five different phases stabilized by the diverse Br-halogen bonds. (a−c) DFT-optimized model of three types of Br-halogen bonds: type-1 halogen bond (single Br-bond), type-2 halogen bond (triangular triple Br-bonds), and type-3 halogen bond (hexagonal sextuple Br-bonds). (d) Molecular spin density at a size of 8 mm × 8 mm in phases 1−5. (e) Corresponding intermolecular interaction energy per molecule in phases 1−4; the dominant intermolecular interactions are added.

covered by ordered molecules, as shown in Figure 2b, c, respectively. Figure 2b shows an enlarged STM image of the Br monolayer. The bottom layer consists of close-packed bright spots (labeled by a blue arrow in Figure 2b), and its measured unit cell is $0.53 \pm 0.02 \times 0.53 \pm 0.02$ nm. The formation of the Br-monolayer results from the evaporation of Br atoms from the 3Br-PTM molecule source in the crucible during thermal evaporation. A few of the 3Br-PTM molecules (labeled by a black arrow) adsorb on the top of the Br-monolayer. DFT calculations in Figure 2d highlight that the Br atoms preferably absorb on the hcp sites of the Au(111) substrate to form a close-packed structure. The calculated unit cell is 0.54 nm × 0.54 nm, which is twice that of the Au(111) substrate lattice (0.27 nm), and this result is comparable to the extracted lattice periodicity (~0.53 nm) from the STM image.

When the molecules were deposited at a lower Knudsen cell temperature of 150 °C, we do not observe a similar 3Br-PTM molecule arrangement, and only the Br sub-monolayer is observed in Figure S2a, suggesting an easier evaporation of Br-atoms than the molecule and leading to the formation of the 3Br-PTM/Br-monolayer/Au(111). The X-ray photoelectron spectroscopy (XPS) measurements of the 3Br-PTM monolayer on the Br-monolayer on Au(111) in Figure S3 also show two distinct Br-3d peaks, which originate from two different chemical states of Br−C and Br−Au bonds, indicating that the Br atom is still bonded onto the molecule.[50] We propose that cross-coupling between Br-terminated PTM molecules takes place in the Knudsen cell, suggested by the color change of the precursor powder. The cross-coupling leads to a higher temperature for the PTM oligomers to evaporate on the surface. Therefore, only intact 3Br-PTM molecules were evaporated on the surface at low temperature. Figure S2b shows that the thickness of the Br monolayer is about 0.13 nm.

We propose the strong adsorption of Br atoms on Au(111), which is also supported by the disappearance of the Au(111) herringbone reconstruction in Figures 2a and S4a.[51,52] In contrast, the 3Br-PTM molecules are not strongly absorbed on the Br-monolayer. The orientation of each individual 3Br-PTM molecule is random, and the corresponding molecular thickness is ~0.28 nm in Figure S2d. We infer that the adsorption of 3Br-PTM molecules on the Br-monolayer is weak physical adsorption. To verify the hypothesis of weak physical adsorption of 3Br-PTM molecules on the Br-monolayer, DFT calculations were performed to estimate the molecular binding energy. Figure 2e shows that the interlayer distance between the 3Br-PTM molecule and Br monolayer is very large (0.51 nm), which is beyond the range of chemisorption, suggesting that the adsorption of the 3Br-PTM molecule on the Br-monolayer is a physisorption process. DFT calculations show that the binding energy of the 3Br-PTM molecule on the Br-monolayer/Au(111) is only ~81 meV per atom, and the absorption energy is reduced by 1% upon 3Br-PTM molecule absorption, verifying that the effect of the Br-monolayer/Au(111) substrate on the molecule is weak. This result is reasonable since the Br-monolayer has a large energy gap and is used as an insulating buffer layer.[53]

Figure 2c displays an enlarged STM image of the 3Br-PTM domain on the Br-monolayer on Au(111). In this domain, a highly ordered molecular array is observed, which is labeled as phase-1. We infer the formation of triple Br-halogen bonds since three terminal Br atoms are adjacent. The DFT-optimized molecular packing structure in Figure 2f supports our STM observation, suggesting that triple Br-halogen bonds govern the self-assembly of the 3Br-PTM molecule into highly ordered molecular spin arrays, as further discussed in Figure 4.

Figure 3 presents the multiphases of 3Br-PTM self-assembled on the Br-monolayer on Au(111) at high molecular coverage. Five molecular self-assembled phases were observed when the molecular coverage is high (∼0.9 mL). Figure 3a represents phase-2 with a highly packed ordered structure at a coverage of ∼0.9 mL. We observe the existence of multiphases, and Figure S5 gives a large-scale STM image of the mixed phase-1 and -2 on the Br-monolayer on Au(111). The high-resolution STM image in Figure 3b shows that six 3Br-PTM molecules form a close-packed ring-like architecture. Figure 3c presents a DFT-optimized structure of phase-2, which reproduces the STM observation. The optimized structure suggests that six Br atoms form a hexagon, and each of these bromine atoms interacts with two neighboring Br atoms through Br-halogen bonds. We infer that the formation of hexagonal sextuple Br-bonds (type-3 halogen bonds) promotes 3Br-PTM molecular assembly into phase-2 molecular spin arrays, as elaborated in Figure 4.

Phase-3 is also observed in other areas, with its hexagonal porous structures. An STM image in Figure 3d shows that phase-3 molecular arrays are regularly distributed with nanopores ∼2.0 nm in diameter. A high-resolution STM image in Figure 3e shows that six 3Br-PTM molecules are assembled into a hexagonal nanopore. The DFT-optimized structure in Figure 3f suggests that each edge of the nanopore consists of two 3Br-PTM molecules that align linearly via a single Br-bond (type-1 halogen bond, as discussed in Figure 4a). Figure S6 displays mixed phase-3 and phase-1 of 3Br-PTM on the Br-monolayer on Au(111). Phase-3 usually forms a small domain, and its structural instability affects the STM-tip state during scanning.

Like phase-3, phase-4 also has a hexagonal porous structure. Figure 3g displays an STM image of the phase-4 molecular array with regularly distributed but isolated nanopores. The enlarged STM image in Figure 3h shows that six 3Br-PTM molecules assembled into a hexagonal nanopore. Unlike phase-3, the porous edges (molecules) in phase-4 are independent and do not share with other nanopores. The DFT-optimized structure in Figure 3i verifies our finding, suggesting that the molecular edge comprises two 3Br-PTM molecules that align linearly via a single Br-bond (type-1 halogen bond, same as phase-3). Furthermore, the DFT-optimized structure suggests the formation of triangular triple Br-bonds (type-2 halogen bond, as observed in phase-1), which bridges the isolated nanopores into 2D porous molecular spin arrays. Figure S7 exhibits a large-scale STM image of phase-4 of 3Br-PTM on the Br-monolayer on Au(111). The high yield of ordered nanostructures indicates that phase-4 has good structural stability.

Phases 1−4 are mixed at high molecular coverage before annealing. Statistically, the yields of phases1−4 are 42, 29, 5, and 24%, respectively. Table S1 summarizes the observed molecular phases at different annealing temperatures. According to Table S1, phases 1, 2, and 4 remain stable below 200 °C. Phase-3 is unstable since it disappears when annealing at 200 °C. Due to its low stability, the statistical yield of phase-3 is only ∼5% at room temperature.

Unexpectedly, a new phase-5 emerges after the sample is annealed at 250 °C. Figure 3j presents the phase-5 molecular array that resembles the Si(111)-(7 × 7) reconstruction-like structure. Figure S8 shows the large-scale STM images of mixed phase-5 and phase-1 of 3Br-PTM on the Br-monolayer on Au(111). A high-resolution STM image in Figure 3k and

the proposed molecular packing structure in Figure 3i suggest that the 3Br-PTM molecules assemble into a Si(111)-(7 × 7) reconstruction-like array, governed by the combination of two types of halogen bonds, namely, the single Br-bond (type-1 halogen bond) and triangular triple Br-bond (type-2 halogen bond). Although the supramolecular arrangements are different, phase-5 and phase-4 are similar in terms of the molecular interactions involved. The Si(111)-(7 × 7) reconstruction-like molecular spin array is obtained in a large scale of 200 nm × 200 nm (Figure S9), indicating that phase-5 is energetically stable.

We infer that the formation of the above multiphases is mainly governed by their diverse intermolecular interactions, while the molecule−substrate interaction does not play an important role in the self-assembled structures. The Br-monolayer is considered an insulating layer that is electronically inactive.[53] DFT calculations also verify that the molecule−substrate interaction of 3Br-PTM on the Br-monolayer is weak (∼81 meV per atom). To understand the inherent mechanism of the formation of the five observed phases, further DFT calculations were performed in order to gain insight into the respective intermolecular interactions.

We studied the three types of molecular interactions that are involved in the five phases, namely, type-1 halogen bond (single Br-bond), type-2 halogen bond (triangular triple Br-bonds), and type-3 halogen bond (hexagonal sextuple Br-bonds), respectively. Figure 4a−c displays the three corresponding optimized models after formation energy minimization. Halogen bonds form based on the mutual interaction between halogen atoms because of the anisotropic distribution of their electron densities.[54,55] The electron density anisotropic distribution leads to the coexistence of electron-depleted σ-holes at the pole of the C−Br bond and encircling electron-rich equatorial belt that is perpendicular to the C−Br bond. Figure 4a shows the type-1 halogen bond where two 3Br-PTM molecules are aligned such that two Br atoms are close. The calculated Br−Br distance (d_1) is about ∼3.8 Å, within the range of short intermolecular interactions, suggesting the formation of halogen bonding interaction. The bond angle (∂_1) is ∼118°. Our experimental observation of type-1 halogen bonds has also been theoretically predicted in 2017.[54] In addition, we propose that the Br−H interaction forms along with type 1−3 halogen bonds. For simplicity, we prefer type 1−3 halogen bonds and do not distinguish the Br−H halogen bonding and the Br−Br halogen bonding.

Type-2 halogen bonds (triangular triple Br-bonds) have been frequently reported.[46,54] Figure 4b shows that three Br atoms are adjacent to each other, and they form a triangle after structural optimization. The bond angle (∂_2) and Br−Br distance (d_2) are ∼60° and ∼3.6 Å, respectively. These parameters are comparable to the reported case.[54] Type-3 hexagonal sextuple Br-bonds are resolved in phase-2. The DFT-optimized model in Figure 4c shows that six Br atoms form a hexagon with a bond angle (∂_3) of ∼119° and a Br−Br distance (d_3) of ∼3.6 Å. The type-3 halogen bond has been theoretically predicted,[54] and it was recently demonstrated by Maier et al. in experiment.[45] The types of halogen bonds are diverse and are realized in a variety of molecular self-assembled structures, thus achieving variable lateral distances of two molecular spins. Here, we record three different distances between two molecular spins: 13.6, 21.3, and 23.1 Å. Moreover, different intermolecular halogen interactions lead to variable molecular spin densities and molecular spin

distances. Figure 4d summarizes the molecular spin densities of the five phases. The maximum molecular spin density of 3×10^{13} at a size of 8 mm × 8 mm is found in highly packed phase-2.

The interaction energy for the four phases is also provided in Figure 4e. We note that the phase interaction energy is correlated with their bond interaction energy with the energy order type-2 > type-3 > type-1. Phase-3 has minimum intermolecular interaction energy compared to the other phases due to the weakest type-1 halogen bond, which further confirms our experimental observation that its statistical yield is the lowest. The type-2 bond is strongest among the three halogen bonds. Thus, the type-2 bond-stabilized phase-1 results in the highest statistical yield. According to the intermolecular interaction energy, we infer an order of structural stability: phase-1 > phase-4 > phase-3, which is consistent with our experimental statistical yield order phase-1 > phase-4 > phase-3.

Based on the DFT calculations and our experimental observations, we infer that the formation of five phases is mainly driven by different types of halogen bonds, and the dominant types of molecular interaction are added in Figure 4e. We note that the formation of halogen bonds/phases depends on the molecular density and annealing temperature. At low coverage, we only observed the existence of phase-1, which may be related to the strong interaction of the type-2 halogen bond. At high coverage, phase-2 is commonly found due to its highest molecular density (fourth row of Table 1)

Table 1. Summary of the Calculated Molecular Interaction Energy, Types of Molecular Interactions, and Molecular Density in Phases 1−5

items	phase-1	phase-2	phase-3	phase-4	phase-5
interaction energy (eV)[a]	−0.229	−0.418	−0.131	−0.167	--
type of molecular interaction	type-2	type-3 and vdW	type-1	type-1 &; type-2	type-1 and type-2
molecular density[b]	409	433	370	392	400

[a]Interaction energy per molecule. [b](molecules/10^3 nm^2).

that leads to the second dominant interaction of the van der Waals force (vdW) force, in addition to the type-2 halogen bond, whereas the other observed phases form locally, which may be because the 3Br-PTM molecules are not uniformly distributed on the surface. Table S1 summarizes the effect of annealing treatment on different self-assembled phases. Upon annealing at 200 °C, phase-3 disappears since the involved type-1 halogen bond is weak, while phases-1, -2, and -4 remain. The emergence of phase-5 with a long-scale order of 200 nm × 200 nm is observed when the sample was annealed at 250 °C.

The intermolecular interaction energy of phase-2 is the highest among the four phases. We attribute this to two origins, type-3 halogen bond and the vdW force. The vdW force also plays an important role in phase-2 due to its highest molecular density, as shown in the third row in Table 1. Phase-4 has moderate intermolecular interaction energy than phase-1 and phase-3 (Table 1 and Figure 4e), which is attributed to a combination of type-1 and type-2 halogen bonds. We cannot obtain the optimized structure of phase-5 since its unit cell is very large and exceeds our available computing capacity. Nevertheless, the molecular interaction energy of phase-5 is

expected to fall in the range of phase-1 and phase-3 since phase-5 is arranged from a combination of type-1 and type-2 halogen bonds, like in the case of phase-4.

In conclusion, 2D supramolecular spin arrays were realized on an insulating Br-monolayer on Au(111). The halogen bonds are the main determinant of the supramolecular spin array formation. By taking advantage of the diversity of halogen bonds, five kinds of 2D molecular spin arrays were achieved with variable molecular spin densities and spin distances. DFT calculations support our STM observations, suggesting that the formation of three types of halogen bonds influences the 2D molecular spin arrays. Our work suggests a supramolecular self-assembly facilitated by halogen bonding as a promising method to engineer low-dimensional molecular spin arrays for potential magnetic device applications. Further works, that is, scanning tunneling spectroscopy/ESR-STM measurements, are needed to reveal the spin-exchange interaction of the molecular spin arrays and individually address (read/write) each molecular spin.[56]

■ ASSOCIATED CONTENT

ⓈI Supporting Information

The Supporting Information is available free of charge at https://pubs.acs.org/doi/10.1021/acsnanoscienceau.2c00005.

Experimental methods—materials, synthesis of precursor, and on-surface preparation of the molecular monolayer; additional STM images; XPS measurement; NMR and MS spectrum; and crystal data (PDF)

■ AUTHOR INFORMATION

Corresponding Authors

Dingguan Wang − *Department of Physics, National University of Singapore, Singapore 117551, Singapore;* ◉ orcid.org/0000-0001-7396-0959; Email: dg.wang@nus.edu.sg

Jishan Wu − *Department of Chemistry, National University of Singapore, Singapore 117543, Singapore;* ◉ orcid.org/0000-0002-8231-0437; Email: chmwuj@nus.edu.sg

Andrew T. S. Wee − *Department of Physics, National University of Singapore, Singapore 117551, Singapore;* ◉ orcid.org/0000-0002-5828-4312; Email: phyweets@nus.edu.sg

Authors

Zishen Wang − *Department of Physics, National University of Singapore, Singapore 117551, Singapore;* ◉ orcid.org/0000-0003-0578-2868

Shaofei Wu − *Department of Chemistry, National University of Singapore, Singapore 117543, Singapore*

Arramel − *Department of Physics, National University of Singapore, Singapore 117551, Singapore;* ◉ orcid.org/0000-0003-4125-6099

Xinmao Yin − *Singapore Synchrotron Light Source (SSLS), National University of Singapore, Singapore 117603, Singapore; Shanghai Key Laboratory of High Temperature Superconductors, Physics Department, Shanghai University, Shanghai 200444, China;* ◉ orcid.org/0000-0002-8246-4444

Chi Sin Tang − *Singapore Synchrotron Light Source (SSLS), National University of Singapore, Singapore 117603, Singapore; Institute of Materials Research and Engineering, A*STAR (Agency for Science, Technology and Research),*

Singapore 138634, Singapore; orcid.org/0000-0002-2414-7192

Yuan Ping Feng − *Department of Physics, National University of Singapore, Singapore 117551, Singapore;* orcid.org/0000-0003-2190-2284

Author Contributions

D.W., Z.W., and S.W. contributed equally to this work. D.W. performed the sample preparation and STM experiments and analyzed the experimental results. D.W., Z.W, S.W, Prof. J.W., and Prof. A.T.S.W. discussed the data. Z.W. performed the first-principles calculations under the supervision of Prof. Y.F.; S.W synthesized the 3Br-PTM molecule under the supervision of Prof. J.W.; D.W., Arramel, Prof. J.W., and Prof. A.T.S.W. wrote the paper, and all authors revised the final manuscript.

REFERENCES

(1) Goodwin, C. A. P.; Ortu, F.; Reta, D.; Chilton, N. F.; Mills, D. P. Molecular Magnetic Hysteresis at 60 Kelvin in Dysprosocenium. *Nature* **2017**, *548*, 439−442.

(2) Guo, F.-S.; Day, B. M.; Chen, Y.-C.; Tong, M.-L.; Mansikkamäki, A.; Layfield, R. A. A Dysprosium Metallocene Single-Molecule Magnet Functioning at the Axial Limit. *Angew. Chem., Int. Ed.* **2017**, *56*, 11445−11449.

(3) Gaita-Ariño, A.; Luis, F.; Hill, S.; Coronado, E. Molecular Spins for Quantum Computation. *Nat. Chem.* **2019**, *11*, 301−309.

(4) Leuenberger, M. N.; Loss, D. Quantum Computing in Molecular Magnets. *Nature* **2001**, *410*, 789−793.

(5) Krainov, I. V.; Klier, J.; Dmitriev, A. P.; Klyatskaya, S.; Ruben, M.; Wernsdorfer, W.; Gornyi, I. V. Giant Magnetoresistance in Carbon Nanotubes with Single-Molecule Magnets Tbpc2. *ACS Nano* **2017**, *11*, 6868−6880.

(6) Pinkowicz, D.; Chorąży, S.; Stefańczyk, O. An Invitation to Molecular Magnetism. *Sci. Prog.* **2011**, *94*, 139−183.

(7) Day, B. M.; Guo, F.-S.; Layfield, R. A. Cyclopentadienyl Ligands in Lanthanide Single-Molecule Magnets: One Ring to Rule Them All? *Acc. Chem. Res.* **2018**, *51*, 1880−1889.

(8) Liu, J.-L.; Chen, Y.-C.; Tong, M.-L. Symmetry Strategies for High Performance Lanthanide-Based Single-Molecule Magnets. *Chem. Soc. Rev.* **2018**, *47*, 2431−2453.

(9) Marin, R.; Brunet, G.; Murugesu, M. Shining New Light on Multifunctional Lanthanide Single-Molecule Magnets. *Angew. Chem., Int. Ed.* **2021**, *60*, 1728−1746.

(10) Yu, K.-X.; Kragskow, J. G. C.; Ding, Y.-S.; Zhai, Y.-Q.; Reta, D.; Chilton, N. F.; Zheng, Y.-Z. Enhancing Magnetic Hysteresis in Single-Molecule Magnets by Ligand Functionalization. *Chem* **2020**, *6*, 1777−1793.

(11) Jin, P. B.; Zhai, Y. Q.; Yu, K. X.; Winpenny, R. E. P.; Zheng, Y. Z. Dysprosiacarboranes as Organometallic Single-Molecule Magnets. *Angew. Chem., Int. Ed.* **2020**, *59*, 9350−9354.

(12) Gopalakrishna, T. Y.; Zeng, W.; Lu, X.; Wu, J.; Wu, J. From Open-Shell Singlet Diradicaloids to Polyradicaloids. *Chem. Commun.* **2018**, *54*, 2186−2199.

(13) Liu, C.; Sandoval-Salinas, M. E.; Hong, Y.; Gopalakrishna, T. Y.; Phan, H.; Aratani, N.; Herng, T. S.; Ding, J.; Yamada, H.; Kim, D.; Casanova, D.; Wu, J. Macrocyclic Polyradicaloids with Unusual Super-Ring Structure and Global Aromaticity. *Chem* **2018**, *4*, 1586−1595.

(14) Katoh, K.; Yamashita, S.; Yasuda, N.; Kitagawa, Y.; Breedlove, B. K.; Nakazawa, Y.; Yamashita, M. Control of the Spin Dynamics of Single-Molecule Magnets by Using a Quasi One-Dimensional Arrangement. *Angew. Chem., Int. Ed.* **2018**, *57*, 9262−9267.

(15) Liu, J.; Ravat, P.; Wagner, M.; Baumgarten, M.; Feng, X.; Müllen, K. Tetrabenzo[a,F,J,O]Perylene: A Polycyclic Aromatic Hydrocarbon with an Open-Shell Singlet Biradical Ground State. *Angew. Chem., Int. Ed.* **2015**, *54*, 12442−12446.

(16) Zeng, W.; Sun, Z.; Herng, T. S.; Gonçalves, T. P.; Gopalakrishna, T. Y.; Huang, K.-W.; Ding, J.; Wu, J. Super-Heptazethrene. *Angew. Chem., Int. Ed.* **2016**, *55*, 8615−8619.

(17) Aulakh, D.; Liu, L.; Varghese, J. R.; Xie, H.; Islamoglu, T.; Duell, K.; Kung, C.-W.; Hsiung, C.-E.; Zhang, Y.; Drout, R. J.; Farha, O. K.; Dunbar, K. R.; Han, Y.; Wriedt, M. Direct Imaging of Isolated Single-Molecule Magnets in Metal−Organic Frameworks. *J. Am. Chem. Soc.* **2019**, *141*, 2997−3005.

(18) Laskowska, M.; Pastukh, O.; Kuźma, D.; Laskowski, Ł. How to Control the Distribution of Anchored, Mn12−Stearate, Single-Molecule Magnets. *Nanomaterials* **2019**, *9*, 1730.

(19) Zhang, X.; Wolf, C.; Wang, Y.; Aubin, H.; Bilgeri, T.; Willke, P.; Heinrich, A. J.; Choi, T. Electron Spin Resonance of Single Iron Phthalocyanine Molecules and Role of Their Non-Localized Spins in Magnetic Interactions. *Nat. Chem.* **2022**, *14*, 59−65.

(20) Gómez-Segura, J.; Veciana, J.; Ruiz-Molina, D. Advances on the Nanostructuration of Magnetic Molecules on Surfaces: The Case of Single-Molecule Magnets (Smm). *Chem. Commun.* **2007**, 3699−3707.

(21) Köbke, A.; Gutzeit, F.; Röhricht, F.; Schlimm, A.; Grunwald, J.; Tuczek, F.; Studniarek, M.; Longo, D.; Choueikani, F.; Otero, E.; Ohresser, P.; Rohlf, S.; Johannsen, S.; Diekmann, F.; Rossnagel, K.; Weismann, A.; Jasper-Toennies, T.; Näther, C.; Herges, R.; Berndt, R.; Gruber, M. Reversible Coordination-Induced Spin-State Switching in Complexes on Metal Surfaces. *Nat. Nanotechnol.* **2020**, *15*, 18−21.

(22) Serrano, G.; Poggini, L.; Briganti, M.; Sorrentino, A. L.; Cucinotta, G.; Malavolti, L.; Cortigiani, B.; Otero, E.; Sainctavit, P.; Loth, S.; Parenti, F.; Barra, A.-L.; Vindigni, A.; Cornia, A.; Totti, F.; Mannini, M.; Sessoli, R. Quantum Dynamics of a Single Molecule Magnet on Superconducting Pb(111). *Nat. Mater.* **2020**, *19*, 546−551.

(23) Cini, A.; Mannini, M.; Totti, F.; Fittipaldi, M.; Spina, G.; Chumakov, A.; Rüffer, R.; Cornia, A.; Sessoli, R. Mössbauer Spectroscopy of a Monolayer of Single Molecule Magnets. *Nat. Commun.* **2018**, *9*, 480.

(24) Mishra, S.; Lohr, T. G.; Pignedoli, C. A.; Liu, J.; Berger, R.; Urgel, J. I.; Müllen, K.; Feng, X.; Ruffieux, P.; Fasel, R. Tailoring Bond Topologies in Open-Shell Graphene Nanostructures. *ACS Nano* **2018**, *12*, 11917−11927.

(25) Liu, J.; Mishra, S.; Pignedoli, C. A.; Passerone, D.; Urgel, J. I.; Fabrizio, A.; Lohr, T. G.; Ma, J.; Komber, H.; Baumgarten, M.; Corminboeuf, C.; Berger, R.; Ruffieux, P.; Müllen, K.; Fasel, R.; Feng, X. Open-Shell Nonbenzenoid Nanographenes Containing Two Pairs

of Pentagonal and Heptagonal Rings. *J. Am. Chem. Soc.* **2019**, *141*, 12011−12020.

(26) Su, J.; Telychko, M.; Hu, P.; Macam, G.; Mutombo, P.; Zhang, H.; Bao, Y.; Cheng, F.; Huang, Z.-Q.; Qiu, Z.; Tan, S. J. R.; Lin, H.; Jelínek, P.; Chuang, F.-C.; Wu, J.; Lu, J. Atomically Precise Bottom-up Synthesis of Π-Extended [5]Triangulene. *Sci. Adv.* **2019**, *5*, No. eaav7717.

(27) Li, J.; Sanz, S.; Castro-Esteban, J.; Vilas-Varela, M.; Friedrich, N.; Frederiksen, T.; Peña, D.; Pascual, J. I. Uncovering the Triplet Ground State of Triangular Graphene Nanoflakes Engineered with Atomic Precision on a Metal Surface. *Phys. Rev. Lett.* **2020**, *124*, 177201.

(28) Pavliček, N.; Mistry, A.; Majzik, Z.; Moll, N.; Meyer, G.; Fox, D. J.; Gross, L. Synthesis and Characterization of Triangulene. *Nat. Nanotechnol.* **2017**, *12*, 308−311.

(29) Gragnaniello, L.; Paschke, F.; Erler, P.; Schmitt, P.; Barth, N.; Simon, S.; Brune, H.; Rusponi, S.; Fonin, M. Uniaxial 2d Superlattice of Fe4 Molecular Magnets on Graphene. *Nano Lett.* **2017**, *17*, 7177−7182.

(30) Paschke, F.; Erler, P.; Enenkel, V.; Gragnaniello, L.; Fonin, M. Bulk-Like Magnetic Signature of Individual Fe4h Molecular Magnets on Graphene. *ACS Nano* **2019**, *13*, 780−785.

(31) Goronzy, D. P.; Ebrahimi, M.; Rosei, F.; Arramel; Fang, Y.; De Feyter, S.; Tait, S. L.; Wang, C.; Beton, P. H.; Wee, A. T. S.; Weiss, P. S.; Perepichka, D. F. Supramolecular Assemblies on Surfaces: Nanopatterning, Functionality, and Reactivity. *ACS Nano* **2018**, *12*, 7445−7481.

(32) Huang, Y. L.; Chen, W.; Li, H.; Ma, J.; Pflaum, J.; Wee, A. T. S. Tunable Two-Dimensional Binary Molecular Networks. *Small* **2010**, *6*, 70−75.

(33) Barth, J. V. Molecular Architectonic on Metal Surfaces. *Annu. Rev. Phys. Chem.* **2007**, *58*, 375−407.

(34) Otero, R.; Gallego, J. M.; de Parga, A. L.; Martín, N.; Miranda, R. Molecular Self-Assembly at Solid Surfaces. *Adv. Mater.* **2011**, *23*, 5148−5176.

(35) Goiri, E.; Borghetti, P.; El-Sayed, A.; Ortega, J. E.; de Oteyza, D. G. Multi-Component Organic Layers on Metal Substrates. *Adv. Mater.* **2016**, *28*, 1340−1368.

(36) Wasio, N. A.; Quardokus, R. C.; Forrest, R. P.; Lent, C. S.; Corcelli, S. A.; Christie, J. A.; Henderson, K. W.; Kandel, S. A. Self-Assembly of Hydrogen-Bonded Two-Dimensional Quasicrystals. *Nature* **2014**, *507*, 86−89.

(37) Cheng, F.; Wu, X.-J.; Hu, Z.; Lu, X.; Ding, Z.; Shao, Y.; Xu, H.; Ji, W.; Wu, J.; Loh, K. P. Two-Dimensional Tessellation by Molecular Tiles Constructed from Halogen−Halogen and Halogen−Metal Networks. *Nat. Commun.* **2018**, *9*, 4871.

(38) Cai, L.; Sun, Q.; Bao, M.; Ma, H.; Yuan, C.; Xu, W. Competition between Hydrogen Bonds and Coordination Bonds Steered by the Surface Molecular Coverage. *ACS Nano* **2017**, *11*, 3727−3732.

(39) Lin, X.; Lu, J. C.; Shao, Y.; Zhang, Y. Y.; Wu, X.; Pan, J. B.; Gao, L.; Zhu, S. Y.; Qian, K.; Zhang, Y. F.; Bao, D. L.; Li, L. F.; Wang, Y. Q.; Liu, Z. L.; Sun, J. T.; Lei, T.; Liu, C.; Wang, J. O.; Ibrahim, K.; Leonard, D. N.; Zhou, W.; Guo, H. M.; Wang, Y. L.; Du, S. X.; Pantelides, S. T.; Gao, H.-J. Intrinsically Patterned Two-Dimensional Materials for Selective Adsorption of Molecules And nanoclusters. *Nat. Mater.* **2017**, *16*, 717−721.

(40) Wang, Q. H.; Hersam, M. C. Room-Temperature Molecular-Resolution Characterization of Self-Assembled Organic Monolayers on Epitaxial Graphene. *Nat. Chem.* **2009**, *1*, 206−211.

(41) Stepanow, S.; Lingenfelder, M.; Dmitriev, A.; Spillmann, H.; Delvigne, E.; Lin, N.; Deng, X.; Cai, C.; Barth, J. V.; Kern, K. Steering Molecular Organization and Host−Guest Interactions Using Two-Dimensional Nanoporous Coordination Systems. *Nat. Mater.* **2004**, *3*, 229−233.

(42) Lin, T.; Shang, X. S.; Adisoejoso, J.; Liu, P. N.; Lin, N. Steering on-Surface Polymerization with Metal-Directed Template. *J. Am. Chem. Soc.* **2013**, *135*, 3576−3582.

(43) Xing, L.; Jiang, W.; Huang, Z.; Liu, J.; Song, H.; Zhao, W.; Dai, J.; Zhu, H.; Wang, Z.; Weiss, P. S.; Wu, K. Steering Two-Dimensional Porous Networks with Σ-Hole Interactions of Br···S and Br···Br. *Chem. Mater.* **2019**, *31*, 3041−3048.

(44) Shang, J.; Wang, Y.; Chen, M.; Dai, J.; Zhou, X.; Kuttner, J.; Hilt, G.; Shao, X.; Gottfried, J. M.; Wu, K. Assembling Molecular Sierpiński Triangle Fractals. *Nat. Chem.* **2015**, *7*, 389−393.

(45) Yang, Z.; Fromm, L.; Sander, T.; Gebhardt, J.; Schaub, T. A.; Görling, A.; Kivala, M.; Maier, S. On-Surface Assembly of Hydrogen- and Halogen-Bonded Supramolecular Graphyne-Like Networks. *Angew. Chem., Int. Ed.* **2020**, *59*, 9549−9555.

(46) Teyssandier, J.; Mali, K. S.; De Feyter, S. Halogen Bonding in Two-Dimensional Crystal Engineering. *ChemistryOpen* **2020**, *9*, 225−241.

(47) Wu, S.; Li, M.; Phan, H.; Wang, D.; Herng, T. S.; Ding, J.; Lu, Z.; Wu, J. Toward Two-Dimensional Π-Conjugated Covalent Organic Radical Frameworks. *Angew. Chem., Int. Ed.* **2018**, *57*, 8007−8011.

(48) Mishra, S.; Yao, X.; Chen, Q.; Eimre, K.; Gröning, O.; Ortiz, R.; Di Giovannantonio, M.; Sancho-García, J. C.; Fernández-Rossier, J.; Pignedoli, C. A.; Müllen, K.; Ruffieux, P.; Narita, A.; Fasel, R. Large Magnetic Exchange Coupling in Rhombus-Shaped Nanographenes with Zigzag Periphery. *Nat. Chem.* **2021**, *13*, 581−586.

(49) Zheng, Y.; Li, C.; Zhao, Y.; Beyer, D.; Wang, G.; Xu, C.; Yue, X.; Chen, Y.; Guan, D.-D.; Li, Y.-Y.; Zheng, H.; Liu, C.; Luo, W.; Feng, X.; Wang, S.; Jia, J. Engineering of Magnetic Coupling in Nanographene. *Phys. Rev. Lett.* **2020**, *124*, 147206.

(50) Smykalla, L.; Shukrynau, P.; Korb, M.; Lang, H.; Hietschold, M. Surface-Confined 2d Polymerization of a Brominated Copper-Tetraphenylporphyrin on Au(111). *Nanoscale* **2015**, *7*, 4234−4241.

(51) Wang, D.; Yang, M.; Arramel; Wu, J.; Wee, A. T. S. Thermally Induced Chiral Aggregation of Dihydrobenzopyrenone on Au(111). *ACS Appl. Mater. Interfaces* **2020**, *12*, 35547−35554.

(52) Huang, Z.; Lin, Y.; Han, C.; Sun, Y.-Y.; Wu, K.; Chen, W. Atomic-Scale Local Work Function Characterizations of Br Islands on Cu(111). *J. Phys. Chem. C* **2021**, *125*, 7944−7949.

(53) Drost, R.; Ojanen, T.; Harju, A.; Liljeroth, P. Topological States in Engineered Atomic Lattices. *Nat. Phys.* **2017**, *13*, 668−671.

(54) Han, Z.; Czap, G.; Chiang, C.-l.; Xu, C.; Wagner, P. J.; Wei, X.; Zhang, Y.; Wu, R.; Ho, W. Imaging the Halogen Bond in Self-Assembled Halogenbenzenes on Silver. *Science* **2017**, *358*, 206−210.

(55) Wang, D.; Wang, Z.; Liu, W.; Arramel; Zhou, J.; Feng, Y. P.; Loh, K. P.; Wu, J.; Wee, A. T. S. Atomic-Level Electronic Properties of Carbon Nitride Monolayers. *ACS Nano* **2020**, *14*, 14008−14016.

(56) Li Huang, Y. L.; Lu, Y.; Niu, T. C.; Huang, H.; Kera, S.; Ueno, N.; Wee, A. T. S.; Chen, W. Reversible Single-Molecule Switching in an Ordered Monolayer Molecular Dipole Array. *Small* **2012**, *8*, 1423−1428.